Check for updates

Small

NANO · MICRO small
www.small-journal.com

RESEARCH ARTICLE

Engineering Charge Transfer of MXene-Hybridized Photocatalysts: An In Situ Kelvin Probe Atomic Force Microscopy Study

Wenkang Xu[1] | Zhiyang Yu[1] | Hongxiao Yang[1] | Xiaoyan An[1] | Chao Peng[2] | Guangxing Yang[3] | Hao-Fan Wang[1] | Yonghai Cao[1] | Hongjuan Wang[1] | Hao Yu[1]

[1]School of Chemistry and Chemical Engineering, South China University of Technology, Guangzhou, China | [2]School of Biotechnology and Health Sciences, Wuyi University, Jiangmen, China | [3]School of Chemistry and Chemical Engineering, Guangzhou University, Guangzhou, China

Correspondence: Hao Yu (yuhao@scut.edu.cn)

Received: 1 November 2025 | **Revised:** 23 January 2026 | **Accepted:** 2 February 2026

Keywords: charge-carrier | KPFM | MXene | surface termination | work function

ABSTRACT

Functioning as nanoscale "conductors", 2D transition metal carbides (MXenes) orchestrate interfacial charge-carrier transport between semiconductors. This capability enables precision-engineered control over photocatalytic processes by regulating charge-carrier separation and migration dynamics. However, existing techniques inadequately resolve photogenerated carrier dynamics, hindering rational MXene photocatalyst design. This study addresses this limitation using in situ nanoscale imaging with Kelvin probe force microscopy (KPFM) on a model TiO_2@MXenes system. We demonstrate that the charge transfer direction is governed by work function (W_F) difference, allowing for utilizing MXenes as electron- or hole-accepter by tuning the work function of MXenes. Glycerol treatment increases surface —OH density, lowering MXene W_F to 1.31 eV and strengthening hole-extracting electric fields. By doing so, Pt/TiO_2 modified with low-W_F MXenes, showing 70.7%–91.7% reduction in charge transfer resistance, displayed the electron-hole transport, which vastly outperforms the electron-electron transport mode. This work offers a quantitative design paradigm linking surface terminations to W_F to carrier transport pathways for developing efficient MXene-based heterojunction photocatalysts.

1 | Introduction

Positioned at semiconductor interfaces, MXenes function as nanoscale "conductors" engineering charge-transport [1, 2]. Benefited from the good electrical conductivity [3], exceptional hydrophilicity [4], and high specific surface area [5], MXenes have emerged as pivotal components in designing advanced heterojunction photocatalysts. These materials enable photocatalytic systems reliant on charge-carrier transport to perform with precision-engineered control, surpassing the limitations of bulk composite [6–8]. Representative examples include $Bi_2S_3/Ti_3C_2T_x$ [9], CdS/Ti_3C_2 [10, 11], $TiO_2/C_3N_4/Ti_3C_2$, CdS@Au/$Ti_{3-x}C_2T_y$, CdS/MoS_2/Ti_3C_2, and CdSe@Ti_3C_2 [12], etc. Among them, MXenes primarily function as anchoring sites for semiconductor photocatalysts [7, 13], complementary light-harvesting components [14], charge-carriers separation enhancers [15, 16], and thermal conductors [17]. Among these roles, the separation of photogenerated charge-carrier (electrons and holes, e^-/h^+) typically governs the rate-determining step in photocatalytic reactions [18, 19]. This highlights MXenes' core advantage as a nanoscale "conductor" orchestrating charge-carriers traffic.

To fully harness MXenes' nanoscale "conductor" role in engineering the flow of charge-carriers during photocatalysis,

© 2026 Wiley-VCH GmbH

research efforts have concentrated on unraveling the mechanisms by which MXenes facilitate charge-carrier transfer [20, 21]. Researchers have employed diverse characterization techniques to elucidate the specific behavior of MXenes in photogenerated charge-carrier separation processes, aiming to facilitate catalyst design and enhance catalytic activity [22]. Computational approaches, along with integrated analytical methods combining work function (W_F) measurements, bandgap characterization, and carrier dynamics analyses, are widely employed to investigate photogenerated carrier separation in MXene-based photocatalysts. However, interpretations regarding the underlying separation mechanisms often diverge across different studies. Wu et al. concluded that Ti_3C_2 MXenes donates electrons and accepts holes, employing PAW-GGA electron density calculations [7]. Conversely, analogous spin-polarized DFT simulations by Han et al. indicated Ti_3C_2 MXenes as an electron conductor [11]. Peng et al. provided experimental evidences revealing that hydroxyl-rich Ti_3C_2 MXenes exhibit low W_F, suggesting its effectiveness in hole separation [21]. It should be noted that theoretical models of computational predictions may oversimplify the complex, heterogeneous surfaces inherent to MXenes [1, 23, 24]. However, the complex surface chemistry of MXenes critically determines the directionality of charge carrier transport. This reveals that the evolution of surface functional groups (e.g., oxygen-containing terminations) plays a pivotal role in modulating charge transfer energy barriers [21, 25].

Current experimental studies largely rely on indirect ex situ characterizations, e.g., ultraviolet photoelectron spectroscopy (UPS) and band structure fitting, to infer terminal group effects. This approach, however, fails to correlate localized structures with carrier transport directionality. Consequently, it results in a lack of direct evidence for elucidating the intricate interfacial charge dynamics, particularly the influence of dynamic surface functional groups. So far, the real-time separation and transport pathways of photogenerated electrons and holes at MXene/semiconductor (e.g., TiO_2) interfaces remain elusive at the nanoscale and under in situ conditions. The inherent complexity of MXene surface functional groups constrains mechanistic studies of these interfacial processes, impeding the rational design of high-performance MXene-based photocatalysts.

In situ experimental validation is therefore essential to guide rational design and advance nanostructured MXene catalysts [26]. For MXene-based photocatalysts with intricate nano/microscale architectures, emerging characterization techniques must not only enable in situ observation, but also achieve direct spatial observation of nano-heterojunctions and nanoscale mapping of photogenerated carrier distributions across individual components [27, 28]. Kelvin Probe Force Microscopy (KPFM) excels in nanoscale surface potential mapping, uniquely characterizing space-charge regions and built-in electric fields in heterojunctions. KPFM has resolved carrier separation in individual $BiVO_4$ particles, guiding rational photocatalyst design [29, 30].

This work establishes a model photocatalytic system based on classical TiO_2@MXenes heterostructures, where MXenes serve as tunable platforms interfacing with semiconductor nanoparticles. Leveraging in situ KPFM nanoscale imaging, we directly elucidate the charge carrier transport mechanisms in these systems, addressing the longstanding controversies regarding carrier transport directions. Through a design paradigm of MXenes linking surface terminations to W_F to carrier transport pathways, we provide experimental guidance for designing high-efficiency MXene heterojunctions by optimizing interfacial band alignment for enhanced charge separation.

2 | Results and Discussion

2.1 | Surface-Engineering of MXenes

The LiF/HCl etching protocol was utilized to transform Ti_3AlC_2 and Nb_2AlC MAXs phases into corresponding MXenes [31]. XRD analysis (Figure 1a,b) revealed a low-angle shift of the (002) diffraction peaks after etching, demonstrating Al-layer extraction and conversion of MAX-phases to $Ti_3C_2T_x$ and Nb_2CT_x MXenes [32]. The sole detection of (002) reflections in these MXenes signifies basal-plane stacking with ordered in-plane orientation of MXene nanosheets. Thermal annealing and glycerol treatment were utilized to enable fine-tuned surface-engineering of MXenes (Figure S1) [24, 33, 34]. By annealing in argon at 530°C for 15 min, the *d*-spacings (002) of $Ti_3C_2T_x$ and Nb_2CT_x decreased from 15.0 to 13.9 Å ($\Delta = -7.3\%$) and 14.1 to 12.4 Å ($\Delta = -12.1\%$), respectively. This contraction is attributed to the extraction of interlayer H_2O molecules during annealing [24]. Crucially, no crystalline oxidative impurities (e.g., TiO_2 or NbO_x) were observed in XRD patterns after either treatment, underscoring structural integrity retention of the surface-engineered MXenes [35].

Comprehensive morphological and crystallographic analysis of surface-engineered MXenes was conducted via high-resolution transmission electron microscope (HRTEM) and atomic force microscopy (AFM). The height distribution maps of AFM (Figure S2) prove that surface engineering does not change the roughness of MXenes surface. Figure S1 reveals that $Ti_3C_2T_x$-derived nanosheets (pristine $Ti_3C_2T_x$, G-$Ti_3C_2T_x$, A-$Ti_3C_2T_x$) maintained lateral sizes around 1 μm, while Nb_2CT_x variants (pristine Nb_2CT_x, G-Nb_2CT_x, A-Nb_2CT_x) retained dimensions above 500 nm. The absence of fragmentation confirms the preservation of sheet morphology without inducing structural degradation. SAED analysis (Figure S1) further demonstrated invariant hexagonal symmetry with clear diffraction patterns, indicative of *hcp* lattice ordering and high crystallinity.

The chemical evolution of surface terminations on surface-engineered MXenes was systematically characterized by X-ray Photoelectron Spectroscopy (XPS). As evidenced by the Ti 2*p* and Nb 3*d* spectra in Figure S3, neither the annealing process nor the glycerol treatment led to the formation of any additional chemical species. Survey spectra (Figure S4) and elemental quantification (Table S1) verify —F/—Cl terminations in LiF/HCl-etched $Ti_3C_2T_x$ and Nb_2CT_x. F content drops by 55.2% (A-$Ti_3C_2T_x$) and 100% (A-Nb_2CT_x), while Cl decreases by 66.4% and 16.8%, respectively, indicating that the annealing process induces significant defunctionalization of —F/—Cl terminations [24, 36]. This reduction correlates with increased oxygen content (Table S1), attributed to the stoichiometric compensation by environmental adsorption of oxygen species onto vacancy sites [37, 38]. High-resolution O 1*s* XPS spectra (Figure 1c,d) reveal distinct oxygen terminations: lattice-bound oxides (M—O_x, M = Ti/Nb), oxygen

16136829, 2026, 20, Downloaded from https://onlinelibrary.wiley.com/doi/10.1002/smll.202513542 by Yonghai Cao - South China University Of Technology , Wiley Online Library on [17/11/2026]. See the Terms and Conditions (https://onlinelibrary.wiley.com/terms-and-conditions) on Wiley Online Library for rules of use; OA articles are governed by the applicable Creative Commons License

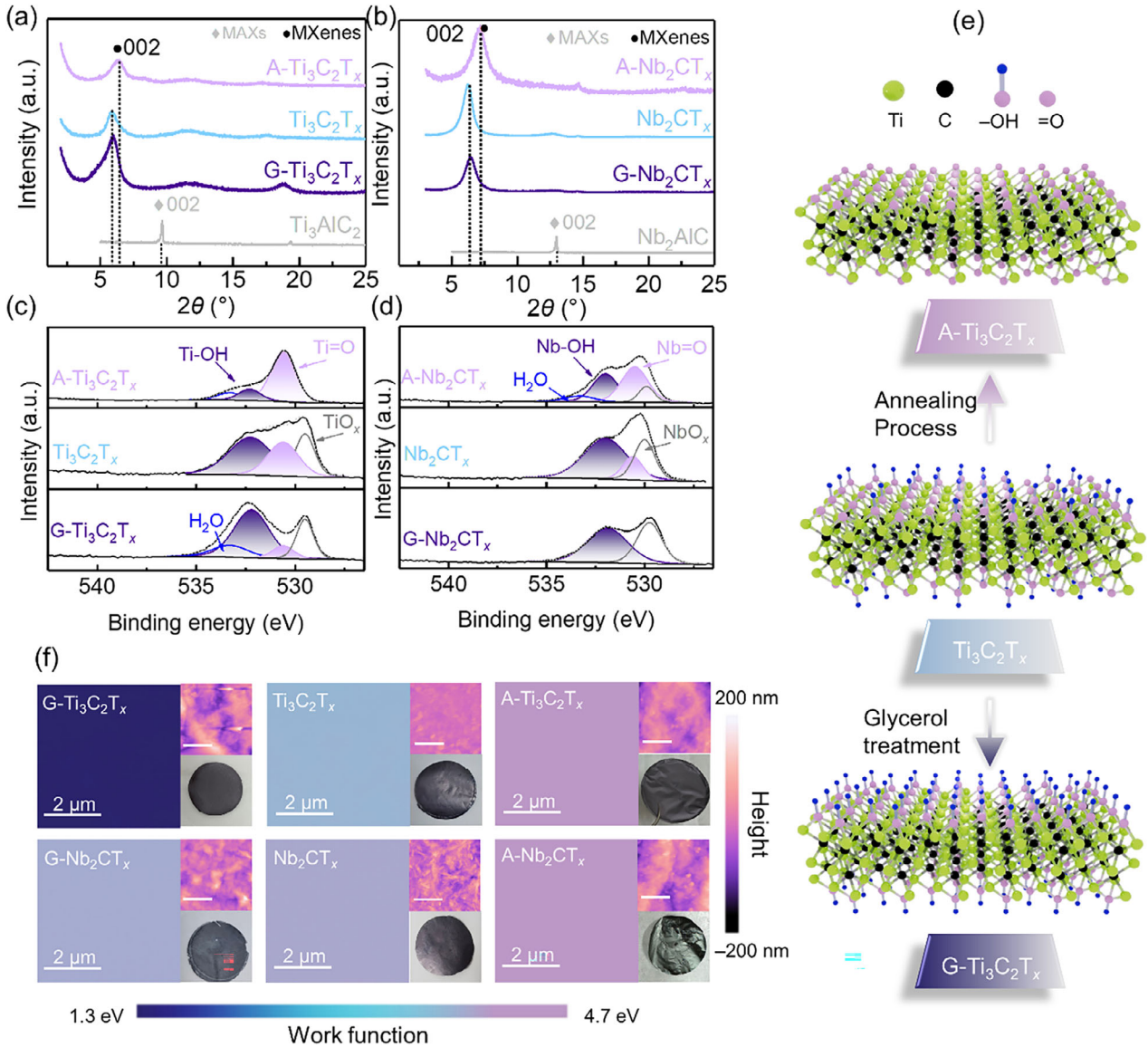

FIGURE 1 | (a,b) XRD patterns, and (c,d) High-resolution O 1*s* XPS spectra of surface-engineered $Ti_3C_2T_x$ and Nb_2CT_x membranes. (e) Schematic diagram for the surface-engineering of MXenes surface functional groups. (f) KPFM surface W_F maps of surface-engineered MXenes. The insets of (f) show the corresponding height maps and freestanding MXene films for W_F measurements. MXenes, A-MXenes, and G-MXenes represent as-prepared MXenes, annealed MXenes, and MXenes treated with glycerol, respectively.

terminations (M═O), hydroxyl groups (M—OH), and adsorbed H_2O (Table S2). After annealing, the ═O/—OH ratio increased dramatically by 7.5-fold for $Ti_3C_2T_x$ and 4.7-fold for Nb_2CT_x (Table S3), indicating thermally driven dehydration of hydroxyl groups (—OH) to terminal oxygen (═O) [39]:

$$Ti_3C_2(OH)_wO_xF_yCl_z \rightarrow Ti_3C_2(OH)_{w-2}O_{x+1} + y/2\ F_2 + z/2\ Cl_2 + H_2O$$

In contrast, glycerol treatment favors hydroxylation, suppressing ═O/—OH to 0.165 (G-$Ti_3C_2T_x$) and eliminating ═O in Nb_2CT_x due to competitive —OH adsorption (Table S3) [34, 40]. The above results demonstrate effective control over the relative content of oxygen-termination through the surface-engineering protocols (Figure 1e).

Surface chemistry dominates 2D MXene nanosheet properties, exemplified by MXenes' W_F sensitivity to terminations [17]. Figure 1f displays W_F distribution maps alongside corresponding height distribution maps, while Table S4 summarizes planar-averaged W_F and root-mean-square roughness (R_q) of W_F for surface-engineered MXenes. Notably, all *R*q values approach zero (Table S4), indicating the homogeneity of W_F characteristics. LiF/HCl-etched $Ti_3C_2T_x$ and Nb_2CT_x exhibit W_Fs of 3.75 eV and 3.93 eV, respectively. Glycerol treatment reduces W_Fs to 1.31 eV (G-$Ti_3C_2T_x$) and 3.88 eV (G-Nb_2CT_x), while the annealing process elevates them to 4.67 eV (A-$Ti_3C_2T_x$) and 4.56 eV (A-Nb_2CT_x). This demonstrates a strong correlation between surface-engineering methods and W_F, with the ═O/—OH ratio acting as a primary regulator (Tables S3 and S4).

Khazaei et al. revealed via DFT that —OH terminations lower W_F (e.g., fully —OH-terminated $Ti_3C_2T_x$: ~1.8 eV), whereas ═O groups increase W_F (up to 6.25 eV) [41]. This phenomenon can be attributed to two main factors: surface dipole effects [42]

16136829, 2026, 20, Downloaded from https://onlinelibrary.wiley.com/doi/10.1002/smll.202513542 by Yonghai Cao - South China University Of Technology , Wiley Online Library on [17/11/2026]. See the Terms and Conditions (https://onlinelibrary.wiley.com/terms-and-conditions) on Wiley Online Library for rules of use; OA articles are governed by the applicable Creative Commons License

and charge redistribution [38]. Regarding the surface dipole effects, electron-donating —OH groups lead to a lowering of the vacuum levels and a reduction in W_F. In contrast, electron-withdrawing =O groups produce the opposite effect. For charge redistribution, —OH groups donate electrons to the M-layers, which raises the Fermi levels and further suppresses the W_F. Conversely, electron-withdrawing =O groups have the opposite impact. Defunctionalization of —Cl/—F minimally impacts W_F due to offsetting dipole and charge effects, compounded by their lower abundance relative to oxygen terminations [38, 41, 42]. Above results confirm that targeted modulation of =O/—OH ratios enable effective W_F control: =O-rich A-MXenes achieve high W_F, while —OH-rich G-MXenes attain ultralow W_F, as summarized in Figure 1e.

2.2 | In Situ KPFM of semiconductor@surface-engineered MXenes

Surface-engineered MXenes with tailored W_F were assembled with TiO_2 (P25) into TiO_2@surface-engineered MXenes heterojunctions to probe charge-carrier transport. TiO_2 nanoparticles were sequentially stacked onto MXene nanosheets pre-coated on mica substrate to simulate photocatalytic heterojunction contacts (Figure 2a; Table S5). AFM height maps and TEM images reveal the $Ti_3C_2T_x$ nanosheets with a thickness of ~1.8 nm and lateral dimensions of hundreds of nanometers (Figures S5 and S6). TiO_2 aggregates display heights up to 60 nm composed of nanoparticles in 10–40 nm diameters (Figures S5 and S6) [43]. For the TiO_2@surface-engineered $Ti_3C_2T_x$ heterojunctions, interfaces between components with pronounced height contrast can be clearly observed (Figure 2b; Figures S5 and S6).

KPFM probes local surface potential distributions by measuring the contact potential difference (CPD) between a conductive probe and the sample [44]. The CPD mapping reveals spatial charge separation (Figure 2c–e), combining with height maps (Figure 2b,f) [29, 45]. Under dark conditions, significant potential differences emerge between TiO_2 and surface-engineered MXenes. G-$Ti_3C_2T_x$ and pristine $Ti_3C_2T_x$ exhibit higher potentials than TiO_2, while A-$Ti_3C_2T_x$ shows a lower potential relative to TiO_2 (Figure 2c,e). This contrast indicates interfacial charge redistribution: electrons transfer from pristine or G-$Ti_3C_2T_x$ to TiO_2 with simultaneous hole migration toward MXenes, and holes move from A-$Ti_3C_2T_x$ to TiO_2 accompanied by electron transfer to the MXenes [30, 46]. To quantify the spatial charge separation, heterojunction contact potential difference (ΔCPD) measurements were performed at designated points on the TiO_2 and surface-engineered MXenes, as indicated by the arrows in Figure 2c,d. A positive ΔCPD indicates higher surface potential on MXenes relative to TiO_2. |ΔCPD| scales proportionally with the extent of interfacial charge redistribution. ΔCPD analysis (Table S6) reveals that TiO_2@G-$Ti_3C_2T_x$ exhibits a 174–175 mV higher ΔCPD_{Dark} than TiO_2@$Ti_3C_2T_x$, confirming enhanced hole conduction of G-$Ti_3C_2T_x$.

Under UV illumination (Figure 2d), the sign of ΔCPD remains unchanged (Table S6), indicating the same charge redistribution direction of TiO_2@surface-engineered $Ti_3C_2T_x$ heterojunction. All heterojunctions show increased |ΔCPD| under UV (Table S6), indicating a light-driven directional carrier migration. The interfacial contact is essential for the charge redistribution. If TiO_2 is spatially isolated from $Ti_3C_2T_x$ nanosheets (>100 nm separation, Figure S7a), no detectable potential difference can be observed ($\Delta CPD_{Light} \approx \Delta CPD_{Dark} \approx 0$ mV) (Figure S7b–d), because the absence of charge-carrier transfer pathways leads to rapid recombination of electrons and holes without altering the interfacial potential equilibrium (Figure S7c,d) [47]. This result suggests that KPFM can be a powerful tool for investigating the interfacial charge-carrier transport in TiO_2@MXenes systems.

Heterojunction surface photovoltage, HSPV = $\Delta CPD_{Light} - \Delta CPD_{Dark}$, is applied to evaluate the directional migration of charge-carrier [48]. Positive HSPV values for TiO_2@G-$Ti_3C_2T_x$ and TiO_2@$Ti_3C_2T_x$ signify the directional migration of photogenerated holes from the semiconductor toward MXenes. Conversely, the negative HSPV of TiO_2@A-$Ti_3C_2T_x$ suggests that A-$Ti_3C_2T_x$ preferentially accepts photogenerated electrons (Figure 2f) [48]. Furthermore, the HSPV of TiO_2@G-$Ti_3C_2T_x$ is approximately 7.75–10.3 times as high as that of TiO_2@$Ti_3C_2T_x$, demonstrating that G-$Ti_3C_2T_x$ exhibits superior hole conductivity compared to pristine $Ti_3C_2T_x$ (Figure 2f) [49]. The reliability of the methodology was verified by systematically varying the structural parameters of the TiO_2@$Ti_3C_2T_x$. As summarized in Figure S8 and Table S6, neither the degree of TiO_2 aggregation (from 80 nm to over 1 μm), nor the TiO_2 particle size (6–25.4 nm), nor the stacked lateral dimensions of the MXene sheets (up to a continuous plane over 5 μm × 5 μm) induced significant changes in the measured ΔCPD or HSPV values. The consistency of the results across these controlled variations confirms the robustness of the in situ KPFM measurements for probing charge transfer in this heterogeneous system.

We extended this methodology to Nb_2CT_x MXenes to probe charge-carrier transport in TiO_2@Nb_2CT_x heterojunctions (Figure S9a and Table S5). KPFM measurements under dark conditions revealed significant potential differences (Figure S9b–d). G-Nb_2CT_x and pristine Nb_2CT_x showed higher potentials than TiO_2, while A-Nb_2CT_x exhibited lower potentials than TiO_2. UV illumination maintained identical carrier migration directions but amplified |ΔCPD| values (Table S7). This confirms interfacial charge redistribution consistent with TiO_2@$Ti_3C_2T_x$ systems (Figure S9e). Positive HSPV in TiO_2@G-Nb_2CT_x/TiO_2@Nb_2CT_x indicated preferential hole conduction of G-Nb_2CT_x and Nb_2CT_x, while negative HSPV in TiO_2@A-Nb_2CT_x demonstrated electron conduction dominance of A-Nb_2CT_x. Notably, TiO_2@G-Nb_2CT_x exhibited a ΔCPD_{Dark} value 7 mV higher than that of TiO_2@Nb_2CT_x, indicating enhanced charge redistribution. HSPV of TiO_2@G-Nb_2CT_x exceeded that of TiO_2@Nb_2CT_x by 1 mV, confirming the superior hole-transport capability of G-Nb_2CT_x (Table S7).

2.3 | Charge Transfer Mechanism

The direction and intensity of charge carrier transport can be elucidated by the W_F-dependence of charge redistribution across the heterojunction. The W_F values of surface-engineered $Ti_3C_2T_x$ and TiO_2 follow the ascending order: G-$Ti_3C_2T_x$ < $Ti_3C_2T_x$ < TiO_2 < A-$Ti_3C_2T_x$ (Figure S10). Thus, A-$Ti_3C_2T_x$, with a higher W_F than TiO_2, preferentially conducts photogenerated electrons, whereas G-$Ti_3C_2T_x$ and pristine $Ti_3C_2T_x$, with a lower W_F than

16136829, 2026, 20, Downloaded from https://onlinelibrary.wiley.com/doi/10.1002/smll.202513542 by Yonghai Cao - South China University Of Technology , Wiley Online Library on [17/11/2026]. See the Terms and Conditions (https://onlinelibrary.wiley.com/terms-and-conditions) on Wiley Online Library for rules of use; OA articles are governed by the applicable Creative Commons License

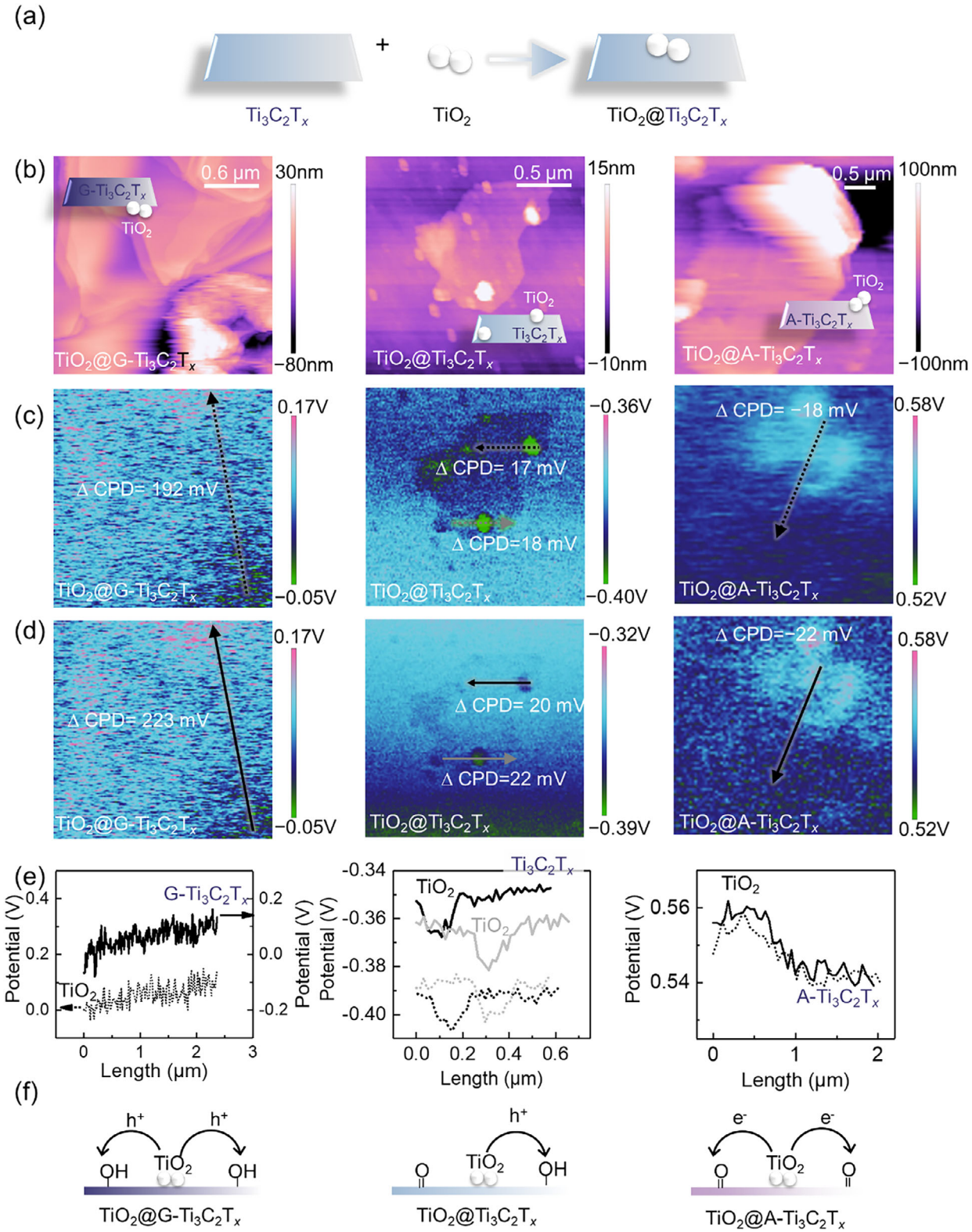

FIGURE 2 | (a) Schematic diagram of TiO_2@$Ti_3C_2T_x$. (b) AFM height distribution images of TiO_2@surface-engineered $Ti_3C_2T_x$. KPFM contact potential difference (CPD) maps of TiO_2@surface-engineered $Ti_3C_2T_x$ (c) in the dark, and (d) under illumination. (e) Surface potential curves along a line in the dark (dashed lines) and under illumination (solid lines) of TiO_2@surface-engineered $Ti_3C_2T_x$ (Arrows pass through the core region of TiO_2 aggregates and pointing toward the MXenes region), (f) Schematic diagrams of carrier transport of TiO_2@surface-engineered $Ti_3C_2T_x$.

16136829, 2026, 20, Downloaded from https://onlinelibrary.wiley.com/doi/10.1002/smll.202513542 by Yonghai Cao - South China University Of Technology , Wiley Online Library on [17/11/2026]. See the Terms and Conditions (https://onlinelibrary.wiley.com/terms-and-conditions) on Wiley Online Library for rules of use; OA articles are governed by the applicable Creative Commons License

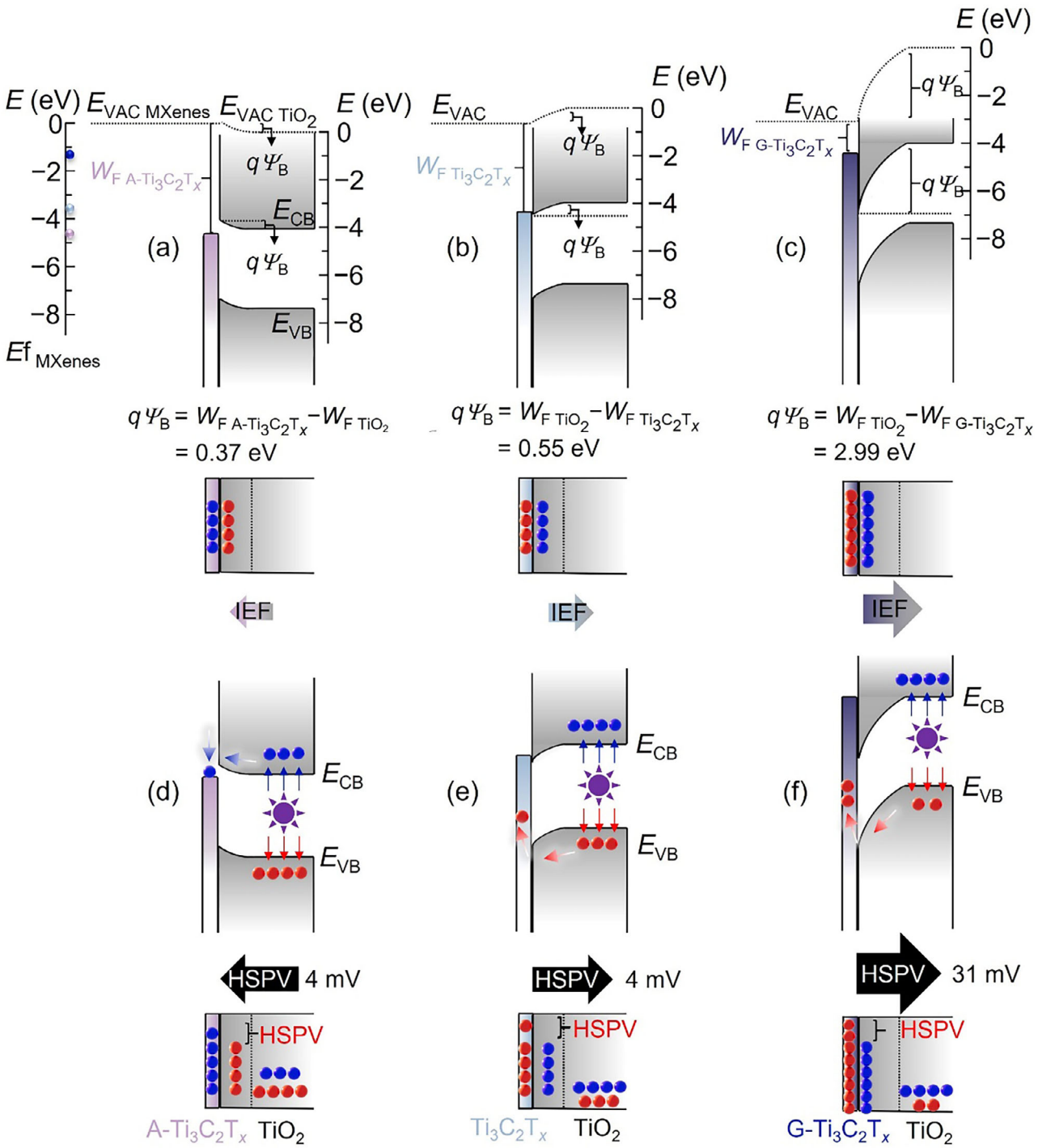

FIGURE 3 | Band structures of TiO_2@surface-engineered $Ti_3C_2T_x$ (a–c) in the dark, and (d–f) under illumination.

TiO_2, facilitate hole transport. Based on the in situ KPFM results, we further analyze the interfacial charge redistribution and carrier transfer dynamics in TiO_2/surface-engineered MXene heterojunctions by resolving their energy band structures.

The interfacial band alignment of surface-engineered MXenes with TiO_2 bifurcates into two distinct configurations according to their relative W_F (Figures S11 and S12). For the high-W_F MXenes, as illustrated in Figure 3a, electrons migrate from TiO_2 to A-$Ti_3C_2T_x$, inducing hole-accumulation layers within TiO_2 and forming a space-charge region. This charge redistribution is experimentally validated by KPFM in Figure 2c. The resultant built-in electric field (IEF), oriented from TiO_2 to A-$Ti_3C_2T_x$ (Figure 3a) [50, 51], drives upward band bending and establishes a Schottky barrier $q\Psi_B$ [52]. For low-W_F MXenes (e.g., TiO_2@G-$Ti_3C_2T_x$), electron transfer from MXenes to TiO_2 induces hole-accumulation layers within MXenes and establishes a negative space-charge region at the TiO_2 interface (Figure 3b,c). The orientation of IEF is from MXenes to TiO_2 (Figure 3b,c). Owing to its larger ΔW_F relative to TiO_2, G-$Ti_3C_2T_x$ enhances interfacial

16136829, 2026, 20, Downloaded from https://onlinelibrary.wiley.com/doi/10.1002/smll.202513542 by Yonghai Cao - South China University Of Technology , Wiley Online Library on [17/11/2026]. See the Terms and Conditions (https://onlinelibrary.wiley.com/terms-and-conditions) on Wiley Online Library for rules of use; OA articles are governed by the applicable Creative Commons License

charge redistribution [53]. KPFM measurements quantitatively confirm this mechanism, revealing a 10.7–11.3 times higher surface potential difference (ΔCPD_{dark}) in TiO_2@G-$Ti_3C_2T_x$ than in TiO_2@$Ti_3C_2T_x$ (Figure 2; Table S6).

The surface-engineering-dependent band alignment results in two distinct carrier transport modes:

(i) Electron-dominant transfer mode

When interfaced with high-W_F A-$Ti_3C_2T_x$, photogenerated electrons traverse the Schottky barrier toward the MXene (Figure 3d). The barrier's rectification effect suppresses electron backflow to TiO_2, inducing negative HSPV (Table S6) [44, 54].

(ii) Hole-dominant transfer mode

For low-W_F G-$Ti_3C_2T_x$ /$Ti_3C_2T_x$ (Figure 3e,f), holes accumulate in the space-charge region under illumination, weakening the Schottky junction [21, 55]. Subsequent hole tunneling transfers holes to the G-$Ti_3C_2T_x$/$Ti_3C_2T_x$, while the barrier blocks hole backflow, leading to hole accumulation and positive HSPV (Table S6) [29]. The ultralow-W_F G-$Ti_3C_2T_x$ enhances the hole-side Schottky barrier height and significantly suppresses hole backflow, boosting hole extraction and separation efficiencies.

To further validate the universality and robustness of the surface-engineering-dependent and W_F-governed charge transfer principle, as shown in Figure S10, we systematically expanded the range of W_F values by preparing additional $Ti_3C_2T_x$ MXenes via a shorter glycerol treatment (G_m-$Ti_3C_2T_x$) and a lower-temperature annealing (A_m-$Ti_3C_2T_x$). We also introduced rutile TiO_2 (R-TiO_2, W_F = 4.06 eV), which has a lower W_F than P25 TiO_2 (TiO_2). KPFM measurements on the corresponding heterojunctions yielded distinct HSPV values (Figure S13 and Table S6). A comprehensive plot of the heterojunction W_F difference against the HSPV, incorporating all previously studied and new cases, reveals a highly significant linear correlation (R^2 = 0.995) (Figure S13d). This robust linear relationship conclusively demonstrates that the proposed charge transfer hypothesis remains valid regardless of whether the W_F variation originates from the MXenes or the TiO_2 component, firmly establishing W_F difference as the primary determinant of charge transfer direction.

2.4 | Optimized MXene-Hybridized Photocatalysts

The two fundamental charge transfer modes allow for the rationale of MXene-hybridized photocatalysts. Our previous Ag/Nb_2O_5@Nb_2CT_x heterostructure adopted an electron-hole (EH) separation mechanism, with Nb_2CT_x as a hole conductor and Ag NPs for electron transfer [56]. Li et al. utilized an electron-electron (EE) separation mechanism to construct CdS@Au/MXenes, where both Au and MXenes transport electrons [8]. In this work, the tunable charge-transfer mechanism offered an opportunity to optimize MXene-based photocatalysts for maximal carrier separation. The systematic evaluation to the photoelectrodes (Figure S14 and Table S8) allows us to compare the design strategies of cocatalysts.

As shown in Figure 4a,b, Figures S15 and S16, surface-engineered MXenes with low W_F ($Ti_3C_2T_x$, G-$Ti_3C_2T_x$, Nb_2CT_x, G-Nb_2CT_x) significantly enhanced the photocurrent of TiO_2, while high-W_F MXenes (A-$Ti_3C_2T_x$, A-Nb_2CT_x) exhibited inferior improvements. This indicates that the low-W_F MXenes more effectively facilitate carrier transfer in TiO_2 than the high-W_F counterparts do [57]. For both bare TiO_2 and Pt/TiO_2 catalysts, hole-conducting G-MXenes outperformed electron-conducting high-W_F A-MXenes in promoting charge-carrier separation. The hydroxyl termination substantially reduces the W_F, thereby strengthening the built-in electric fields. The optimal charge separation performance of G-MXenes suggests that the surface chemistry of MXenes as co-catalysts can be a powerful tool to modify the photocatalytic performance. This carrier-transfer advantage of low-W_F MXenes is further reflected in their reduction kinetics. Linear sweep voltammetry (LSV) curves (Figure S15) confirm that the cathodic current is dominated by the hydrogen evolution reaction (HER) upon loading MXenes. Notably, samples with low-W_F MXenes exhibit a significantly higher current response than those with high-W_F ones, consistent with their superior efficacy in promoting carrier transfer and separation within TiO_2 for HER. While high-W_F MXenes provide a lesser current enhancement, their electron-directing tendency concurrently suppresses the competing surface reduction of TiO_2 (e.g., Ti^{4+} to Ti^{3+}) (Figure S15).

Electrochemical impedance spectroscopy (EIS) and further impedance analysis validated the dynamics of charge-carrier separation (Figure 4c,d; Table S9) [21]. For the EE separation mechanism, Pt/TiO_2@A-MXenes reduced charge transfer resistance (R_{ct}) by 23.7%–53.8% vs. Pt/TiO_2. In contrast, the EH separation mechanism achieved significantly higher R_{ct} reduction, Pt/TiO_2@MXenes reduced R_{ct} by 70.7%–89.8%, while Pt/TiO_2@G-MXenes achieved 90.2%–91.7% reduction, demonstrating superior hole extraction via enhanced interfacial fields. The higher R_{ct} reduction with EH-based designs aligns with reports that hole mobility lags electron mobility by 2–3 orders of magnitude, slow hole transfer increases recombination risks [58]. Low-W_F MXenes address this bottleneck by providing efficient hole-conducting pathways, surpassing electron-focused EE strategies. Among them, Ultralow-W_F G-MXenes induce higher Schottky barriers and built-in fields, maximizing carrier separation (Figure 4e).

3 | Conclusion

To summarize, in situ KPFM definitively resolves longstanding controversies in MXene charge-carrier transfer mechanisms. Direct nanoscale imaging reveals that W_F differences govern carrier transport direction—high-W_F MXenes accept electrons while low-W_F variants conduct holes. For MXene-based heterojunction designs, the electron-hole (EH) transport significantly outperforms the electron-electron (EE) pathways, reducing charge-transfer resistance by up to 91.7%. Critically, glycerol-induced —OH termination lowers the W_F to 1.31 eV, thereby strengthening built-in electric fields for enhanced charge separation. Collectively, the spatial dynamics of charge-distribution revealed by KPFM inspired an unambiguous paradigm linking surface termination of MXenes to W_F and to carrier transport, for designing efficient MXenes heterojunctions through optimized interfacial band alignment.

16136829, 2026, 20, Downloaded from https://onlinelibrary.wiley.com/doi/10.1002/smll.202513542 by Yonghai Cao - South China University Of Technology , Wiley Online Library on [17/11/2026]. See the Terms and Conditions (https://onlinelibrary.wiley.com/terms-and-conditions) on Wiley Online Library for rules of use; OA articles are governed by the applicable Creative Commons License

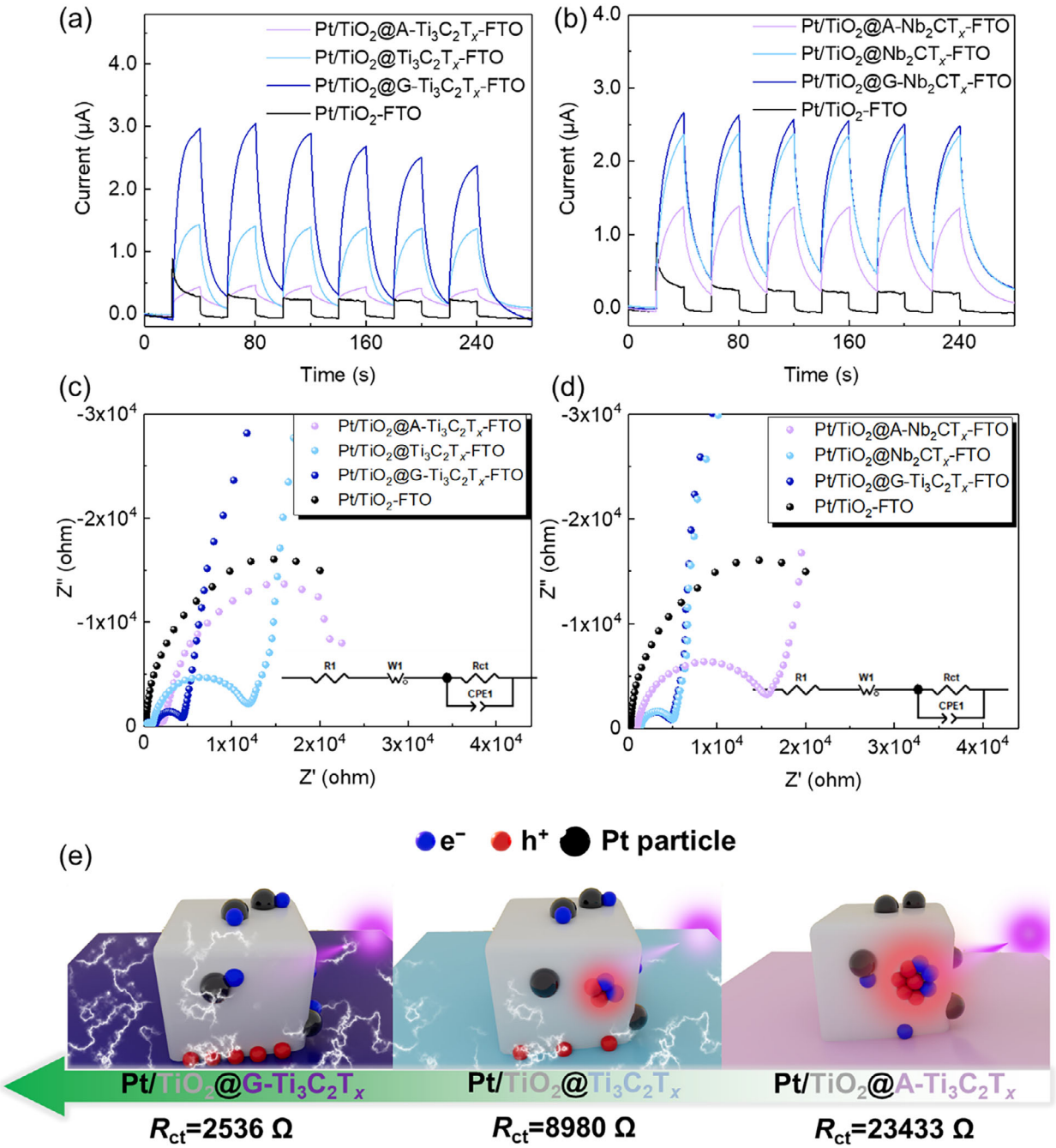

FIGURE 4 | (a,b) Transient photocurrent (I-T) curves of Pt/TiO_2-FTO and Pt/TiO_2@surface-engineered MXenes-FTO. (c,d) Nyquist plots on Pt/TiO_2-FTO and Pt/TiO_2@surface-engineered MXenes-FTO. (e) Schematic diagrams of directional migration and recombination of photogenerated carriers of Pt/TiO_2@surface-engineered $Ti_3C_2T_x$.

4 | Experimental Section

4.1 | Materials

The MAX phases ceramics were purchased from Jilin 11 Technology Co., Ltd., and used as received. The Ti_3AlC_2 and Nb_2AlC were in 200 mesh. P25 (99.5%), S-TiO_2 (99.5%), rutile TiO_2 (99.5%), LiF (AR, 99%), NaCl (Ar, 99.5%), $H_2PtCl_6{\cdot}xH_2O$ (38% Pt basis), and glycerol (AR, 99.0%) were purchased from Shanghai Aladdin Bio-Chem Technology Co., LTD. HCl (36.5%–38%) was purchased from Guangzhou Guangshi Chemical Reagent Co., Ltd. PES (0.22 μm pore size and diameter of 50 mm) membranes were purchased from Jinteng Experimental Equipment Co., Ltd.

4.2 | Methods

4.2.1 | Synthesis of $Ti_3C_2T_x$

$Ti_3C_2T_x$ was synthesized following the LiF/HCl etching method developed by Gogotsi, Barsoum, and co-workers [31], which yields large MXene flakes suitable for structural characterization by KPFM. Briefly, LiF (3.2 g) was dissolved in HCl

16136829, 2026, 20, Downloaded from https://onlinelibrary.wiley.com/doi/10.1002/smll.202513542 by Yonghai Cao - South China University Of Technology , Wiley Online Library on [17/11/2026]. See the Terms and Conditions (https://onlinelibrary.wiley.com/terms-and-conditions) on Wiley Online Library for rules of use; OA articles are governed by the applicable Creative Commons License

(40 mL, 9 M). The mixture was transferred to a Teflon-lined autoclave, after which Ti_3AlC_2 (0.8 g) powder was added incrementally under constant stirring. The reaction proceeded at 45°C for 24 h. The resulting suspension was centrifuged at 5000 rpm for 1 min, and the colorless supernatant was discarded. The sediment was repeatedly washed with deionized water via centrifugation cycles until the supernatant exhibited a black coloration. The black supernatant was then collected and sonicated for 1 min under argon atmosphere, followed by centrifugation at 3500 rpm for 15 min to obtain an ink-like $Ti_3C_2T_x$ dispersion. To prepare freestanding films, the $Ti_3C_2T_x$ ink (2 mL) was vacuum-filtered through a PES membrane and dried at room temperature for 12 h. The freestanding $Ti_3C_2T_x$ film was subsequently delaminated from the PES membrane. Based on the mass of the obtained film (50.8 mg), the concentration of the $Ti_3C_2T_x$ dispersion was determined to be 25.4 mg·mL^{-1}.

4.2.2 | Synthesis of Nb_2CT_x

Nb_2CT_x was synthesized using an identical protocol to that described for **Synthesis of $Ti_3C_2T_x$**: Freestanding Nb_2CT_x films were prepared from the Nb_2CT_x ink (7.2 mL). The mass of the obtained film was 50.8 mg, corresponding to a dispersion concentration of 7.1 mg·mL^{-1}.

4.2.3 | Preparation of Surface-Engineered MXenes

Surface-engineered MXenes were performed to modulate their surface chemistries through thermal annealing and glycerol treatment. Specific conditions and protocols are summarized in Table S10.

4.2.4 | Fabrication of TiO_2@Surface-Engineered MXenes for KPFM Characterization

TiO_2@surface-engineered MXenes were fabricated using a sequential stacking method to sequentially deposit TiO_2 nanoparticles and various surface-engineered MXenes nanosheets. All TiO_2@surface-engineered MXenes assemblies were fabricated on freshly cleaved mica substrates. A schematic illustration of the preparation process for TiO_2@$Ti_3C_2T_x$ is presented in Figure 2a, with detailed protocols provided in Table S5. The mica substrates were cleaved and cut into 0.5 × 0.5 cm^2 squares prior to use. Both surface-engineered MXenes dispersions and TiO_2 colloidal dispersions were diluted to 1 μg mL^{-1} for deposition. Among them, the diluted dispersion of G-MXenes requires the removal of the glycerol step. G-MXenes glycerol dispersion was centrifuged at 12 000 rpm for 10 min. The precipitate was washed and redispersed in DI water to prepare a 1 μg mL^{-1} aqueous dispersion.

Following assembly, the TiO_2@MXenes samples were subjected to annealing at 530°C under argon atmosphere to yield TiO_2@A-MXenes, with annealing parameters documented in Table S5.

4.2.5 | Fabrication of Photoanodes for (Photo)electrochemical Testing

Pt/TiO_2 Preparation Pt/TiO_2 was synthesized via photodeposition. Briefly, TiO_2 powder (100 mg) was dispersed in deionized water (100 mL), followed by the addition of H_2PtCl_6 solution (2 mL, 2 g·L^{-1} Pt). The suspension was irradiated for 6 h under a 300 W xenon lamp. The resulting Pt/TiO_2 was collected by filtration, washed thoroughly with deionized water, and dried overnight at 60°C.

TiO_2-FTO Photoanodes TiO_2 colloidal dispersion (20 μL, 0.5 mg·mL^{-1}) was uniformly drop-cast onto the conductive side of FTO glass and dried overnight in a dust-free environment.

Pt/TiO_2-FTO Photoanodes Pt/TiO_2 colloidal dispersion (20 μL, 0.5 mg·mL^{-1}) was uniformly drop-cast onto the conductive side of FTO glass and dried overnight in a dust-free environment.

Surface-Engineered MXene-Based Photoanodes These photoanodes were fabricated by sequentially depositing MXenes nanosheets and TiO_2 nanoparticles onto FTO substrates via a sequential stacking method (Figure S14). Detailed protocols are provided in Table S8.

FTO Thermal Stability Verification Control experiments confirmed that FTO glass maintained stable surface resistivity after 4 h of annealing at 530°C, demonstrating its compatibility with the 15 min thermal treatments employed in this study.

4.3 | Characterization

4.3.1 | X-ray Diffraction (XRD)

The crystal structure of materials was analyzed in an X-ray powder diffractometer (XRD, X'Pert3 Powder, PANalytical) using Cu Kα radiation ($\lambda = 1.54$ Å) with 0.131° 2θ steps.

4.3.2 | X-ray Photoelectron Spectroscopy (XPS)

X-ray photoelectron spectroscopy (XPS) was measured in a Thermo Scientific K-Alpha+ spectrometer. A monochromatic Al Kα X-ray source (photon energy = 1486.6eV) was used for excitation. The binding energy was corrected by C1s peak at 284.8 eV.

4.3.3 | Transmission Electron Microscopy (TEM)

Transmission electron microscopy images and element contents were obtained in a transmission electron microscope (TEM, JEOL JEM-2100F) using an accelerating voltage of 200 kV.

4.3.4 | Ultraviolet Visible Diffuse Reflection Spectrum (DRUV-Vis)

The UV–vis diffuse reflectance spectroscopy of the catalysts was characterized by a UV–vis spectrophotometer (DRS, U-3010).

16136829, 2026, 20, Downloaded from https://onlinelibrary.wiley.com/doi/10.1002/smll.202513542 by Yonghai Cao - South China University Of Technology , Wiley Online Library on [17/11/2026]. See the Terms and Conditions (https://onlinelibrary.wiley.com/terms-and-conditions) on Wiley Online Library for rules of use; OA articles are governed by the applicable Creative Commons License

4.3.5 | Photoelectrochemical Measurement

The Mott-Schottky, the transient photocurrent spectroscopy (I-T), the linear sweep voltammetry (LSV), and the electrochemical impedance spectroscopy (EIS) were carried out in 2.0 M NaCl aqueous solution with a standard three electrode system equipped with CHI660e electrochemical workstation. A carbon rod was used as the counter electrode, and an Ag/AgCl electrode was used as the reference electrode. The electrochemical performance test was performed at 25°C with potential calibrated to a reversible hydrogen electrode (NHE):

$$E(\mathrm{NHE}) = E(\mathrm{Ag/AgCl}) + 0.197$$

4.3.6 | Atomic Force Microscope (AFM) and Kelvin Probe Force Microscopy (KPFM)

Surface topography and electrical properties were characterized using a Bruker Dimension ICON atomic force microscope (AFM) equipped with a KPFM module. All measurements employed conductive Pt/Ir-coated silicon probes (SCM-PIT-V2; tip diameter: 20 nm, spring constant: 3 $N \cdot m^{-1}$, resonant frequency: 75 kHz) in amplitude-modulation contact mode. The lift height was maintained at 120–300 nm during scans.

All specimens were mounted on metal sample stages using conductive adhesive. The W_F of KPFM tip was calibrated against freshly cleaved highly oriented pyrolytic graphite (HOPG, W_F = 4.60 eV) before each measurement session. Simultaneous surface topography and work function mapping (or contact potential difference (CPD) distribution) was automatically generated by the instrument during scanning.

4.4 | Statistical Analysis

4.4.1 | Pre-Processing of Data

Data obtained from XRD, AFM, KPFM, XPS, and electrochemical measurements were processed with minimal pre-processing. For KPFM measurements, the W_F and CPD values were obtained directly from the instrument's software (Bruker NanoScope Analysis). For XPS analysis, peak deconvolution was performed using standard software packages with Shirley-type background subtraction.

4.4.2 | Data Presentation

Quantitative data were presented as mean values derived from mapping or repeated measurements, as specified. Specifically:

The average surface W_F values and their corresponding R_q for MXenes were reported as the mean calculated from the KPFM map area. The ΔCPD and HSPV values were presented as measured values from line profiles across specific interfaces in the KPFM images. In cases where multiple measurements were made on the same sample type (e.g., TiO_2@$Ti_3C_2T_x$), all obtained values were reported.

4.4.3 | Software Used for Statistical Analysis

The primary software used for data acquisition and analysis included: Jade, Bruker NanoScope Analysis, XPS Peak, CHI660e electrochemical workstation software, and OriginPro.

Acknowledgements

The work was supported by the National Natural Science Foundation of China (No. 22272056), Natural Science Foundation of Guangdong Province (No. 2024B1515040016).

Funding

The work was supported by the National Natural Science Foundation of China (No. 22272056), Natural Science Foundation of Guangdong Province (No. 2024B1515040016).

Conflicts of Interest

The authors declare no conflicts of interest.

Data Availability Statement

The data that support the findings of this study are available from the corresponding author upon reasonable request.

References

1. A. VahidMohammadi, J. Rosen, and Y. Gogotsi, "The World of Two-Dimensional Carbides and Nitrides (MXenes)," *Science* 372, no. 6547 (2021): abf1581, https://doi.org/10.1126/science.abf1581.

2. V. Kamysbayev, A. S. Filatov, H. Hu, et al., "Covalent Surface Modifications and Superconductivity of Two-Dimensional Metal Carbide MXenes," *Science* 369, no. 6506 (2020): 979–983, https://doi.org/10.1126/science.aba8311.

3. F. Shahzad, A. Iqbal, H. Kim, and C. M. Koo, "2D Transition Metal Carbides (MXenes): Applications as an Electrically Conducting Material," *Advanced Materials* 32, no. 51 (2020): 2002159, https://doi.org/10.1002/adma.202002159.

4. Y. Wang, Y. Yue, F. Cheng, et al., "$Ti_3C_2T_x$ MXene-Based Flexible Piezoresistive Physical Sensors," *ACS Nano* 16, no. 2 (2022): 1734–1758, https://doi.org/10.1021/acsnano.1c09925.

5. K. R. G. Lim, A. D. Handoko, S. K. Nemani, et al., "Rational Design of Two-Dimensional Transition Metal Carbide/Nitride (MXene) Hybrids and Nanocomposites for Catalytic Energy Storage and Conversion," *ACS Nano* 14, no. 9 (2020): 10834–10864, https://doi.org/10.1021/acsnano.0c05482.

6. F. He, B. Zhu, B. Cheng, J. Yu, W. Ho, and W. Macyk, "2D/2D/0D $TiO_2/C_3N_4/Ti_3C_2$ MXene Composite S-Scheme Photocatalyst with Enhanced CO_2 Reduction Activity," *Applied Catalysis B: Environmental* 272 (2020): 119006, https://doi.org/10.1016/j.apcatb.2020.119006.

7. C. Wu, W. Huang, H. Liu, K. Lv, and Q. Li, "Insight into Synergistic Effect of Ti_3C_2 MXene and MoS_2 on Anti-Photocorrosion and Photocatalytic of CdS for Hydrogen Production," *Applied Catalysis B: Environmental* 330 (2023): 122653, https://doi.org/10.1016/j.apcatb.2023.122653.

8. Z. Li, W. Huang, J. Liu, K. Lv, and Q. Li, "Embedding CdS@Au into Ultrathin $Ti_{3-x}C_2T_y$ to Build Dual Schottky Barriers for Photocatalytic H_2 Production," *ACS Catalysis* 11, no. 14 (2021): 8510–8520, https://doi.org/10.1021/acscatal.1c02018.

9. J. Li, Z. Li, X. Liu, et al., "Interfacial Engineering of $Bi_2S_3/Ti_3C_2T_x$ MXene Based on Work Function for Rapid Photo-Excited

16136829, 2026, 20, Downloaded from https://onlinelibrary.wiley.com/doi/10.1002/smll.202513542 by Yonghai Cao - South China University Of Technology , Wiley Online Library on [17/11/2026]. See the Terms and Conditions (https://onlinelibrary.wiley.com/terms-and-conditions) on Wiley Online Library for rules of use; OA articles are governed by the applicable Creative Commons License

Bacteria-Killing," *Nature Communications* 12, no. 1 (2021): 1224, https://doi.org/10.1038/s41467-021-21435-6.

10. R. Xiao, C. Zhao, Z. Zou, et al., "In Situ Fabrication of 1D CdS Nanorod/2D Ti_3C_2 MXene Nanosheet Schottky Heterojunction toward Enhanced Photocatalytic Hydrogen Evolution," *Applied Catalysis B: Environment and Energy* 268 (2020): 118382, https://doi.org/10.1016/j.apcatb.2019.118382.

11. Y. Han, L. Ye, T. Gong, and Y. Fu, "Surface-Controlled CdS/Ti_3C_2 MXene Schottky Junction for Highly Selective and Active Photocatalytic Dehydrogenation-Reductive Amination," *Angewandte Chemie International Edition* 62, no. 45 (2023): 202306305, https://doi.org/10.1002/anie.202306305.

12. H. Gu, H. Zhang, X. Wang, et al., "Robust Construction of CdSe Nanorods@Ti_3C_2 MXene Nanosheet for Superior Photocatalytic H_2 Evolution," *Applied Catalysis B: Environmental* 328 (2023): 122537, https://doi.org/10.1016/j.apcatb.2023.122537.

13. L. Yang, W. Liu, T. Hang, L. Wu, and X. Yang, "Roles of MXenes in Photocatalysis," *Solar RRL* 8, no. 1 (2024): 2300691, https://doi.org/10.1002/solr.202300691.

14. C. Jin, D. Sun, Z. Sun, et al., "Interfacial Engineering of Ni-Phytate and $Ti_3C_2T_x$ MXene-Sensitized TiO_2 toward Enhanced Sterilization Efficacy under 808 Nm NIR Light Irradiation," *Applied Catalysis B: Environmental* 330 (2023): 122613, https://doi.org/10.1016/j.apcatb.2023.122613.

15. Q. Xi, F. Xie, J. Liu, et al., "In Situ Formation $ZnIn_2S_4$ /Mo_2TiC_2 Schottky Junction for Accelerating Photocatalytic Hydrogen Evolution Kinetics: Manipulation of Local Coordination and Electronic Structure," *Small* 19, no. 24 (2023): 2300717, https://doi.org/10.1002/smll.202300717.

16. Z. Zhang, B. Wang, H. Zhao, et al., "Self-Assembled Lead-Free Double Perovskite-MXene Heterostructure with Efficient Charge Separation for Photocatalytic CO_2 Reduction," *Applied Catalysis B: Environmental* 312 (2022): 121358, https://doi.org/10.1016/j.apcatb.2022.121358.

17. D. Xu, Z. Li, L. Li, and J. Wang, "Insights into the Photothermal Conversion of 2D MXene Nanomaterials: Synthesis, Mechanism, and Applications," *Advanced Functional Materials* 30, no. 47 (2020): 2000712, https://doi.org/10.1002/adfm.202000712.

18. A. Meng, L. Zhang, B. Cheng, and J. Yu, "Dual Cocatalysts in TiO_2 Photocatalysis," *Advanced Materials* 31, no. 30 (2019): 1807660, https://doi.org/10.1002/adma.201807660.

19. J. Low, J. Yu, M. Jaroniec, S. Wageh, and A. A. Al-Ghamdi, "Heterojunction Photocatalysts," *Advanced Materials* 29, no. 20 (2017): 1601694, https://doi.org/10.1002/adma.201601694.

20. J. Ran, G. Gao, F. Li, T. Ma, A. Du, and S. Qiao, "Ti_3C_2 MXene Co-Catalyst on Metal Sulfide Photo-Absorbers for Enhanced Visible-Light Photocatalytic Hydrogen Production," *Nature Communications* 8, no. 1 (2017): 13907, https://doi.org/10.1038/ncomms13907.

21. C. Peng, P. Wei, X. Li, et al., "High Efficiency Photocatalytic Hydrogen Production over Ternary Cu/TiO_2@$Ti_3C_2T_x$ Enabled by Low-Work-Function 2D Titanium Carbide," *Nano Energy* 53 (2018): 97–107, https://doi.org/10.1016/j.nanoen.2018.08.040.

22. C. Lin, J. Rohilla, H. Kuo, et al., "Density-Functional Theory Studies on Photocatalysis and Photoelectrocatalysis: Challenges and Opportunities," *Solar RRL* 8, no. 10 (2024): 2300948, https://doi.org/10.1002/solr.202300948.

23. Y. Wei, P. Zhang, R. A. Soomro, Q. Zhu, and B. Xu, "Advances in the Synthesis of 2D MXenes," *Advanced Materials* 33, no. 39 (2021): 2103148, https://doi.org/10.1002/adma.202103148.

24. J. L. Hart, K. Hantanasirisakul, A. C. Lang, et al., "Control of MXenes' electronic Properties through Termination and Intercalation," *Nature Communications* 10, no. 1 (2019): 522, https://doi.org/10.1038/s41467-018-08169-8.

25. P. Wei, Y. Chen, T. Zhou, et al., "Manipulation of Charge-Transfer Kinetics via $Ti_3C_2T_x$ (T = −O) Quantum Dot and N-Doped Carbon Dot Coloading on CdS for Photocatalytic Hydrogen Production," *ACS Catalysis* 13, no. 1 (2023): 587–600, https://doi.org/10.1021/acscatal.2c04632.

26. S. C. Warren, K. Voïtchovsky, H. Dotan, et al., "Identifying Champion Nanostructures for Solar Water-Splitting," *Nature Materials* 12, no. 9 (2013): 842–849, https://doi.org/10.1038/nmat3684.

27. W. Zeng, X. Ye, Y. Dong, et al., "MXene for Photocatalysis and Photothermal Conversion: Synthesis, Physicochemical Properties, and Applications," *Coordination Chemistry Reviews* 508 (2024): 215753, https://doi.org/10.1016/j.ccr.2024.215753.

28. R. Chen, F. Fan, and C. Li, "Unraveling Charge-Separation Mechanisms in Photocatalyst Particles by Spatially Resolved Surface Photovoltage Techniques," *Angewandte Chemie International Edition* 61, no. 16 (2022): 202117567, https://doi.org/10.1002/anie.202117567.

29. R. Chen, Z. Ren, Y. Liang, et al., "Spatiotemporal Imaging of Charge Transfer in Photocatalyst Particles," *Nature* 610, no. 7931 (2022): 296–301, https://doi.org/10.1038/s41586-022-05183-1.

30. J. Zhu, F. Fan, R. Chen, H. An, Z. Feng, and C. Li, "Direct Imaging of Highly Anisotropic Photogenerated Charge Separations on Different Facets of a Single $BiVO_4$ Photocatalyst," *Angewandte Chemie International Edition* 54, no. 31 (2015): 9111–9114, https://doi.org/10.1002/anie.201504135.

31. M. Ghidiu, M. R. Lukatskaya, M. Zhao, Y. Gogotsi, and M. W. Barsoum, "Conductive Two-Dimensional Titanium Carbide 'Clay' with High Volumetric Capacitance," *Nature* 516, no. 7529 (2014): 78–81, https://doi.org/10.1038/nature13970.

32. M. Naguib, M. Kurtoglu, V. Presser, et al., "Two-Dimensional Nanocrystals Produced by Exfoliation of Ti_3AlC_2," *Advanced Materials* 23, no. 37 (2011): 4248–4253, https://doi.org/10.1002/adma.201102306.

33. H. Fang, A. Thakur, A. Zahmatkeshsaredorahi, et al., "Stabilizing $Ti_3C_2T_x$ MXene Flakes in Air by Removing Confined Water," *Proceedings of the National Academy of Sciences* 121, no. 28 (2024): 2400084121, https://doi.org/10.1073/pnas.2400084121.

34. P. Tian, G. Yu, K. Wei, Z. Zhang, and N. Wang, "Effect of Hydroxyl Intercalation on Tribological Properties of MXene ($Ti_3C_2T_x$)," *Ceramics International* 47, no. 21 (2021): 30722–30728, https://doi.org/10.1016/j.ceramint.2021.07.251.

35. L. Ding, Y. Wei, L. Li, et al., "MXene Molecular Sieving Membranes for Highly Efficient Gas Separation," *Nature Communications* 9, no. 1 (2018): 155, https://doi.org/10.1038/s41467-017-02529-6.

36. K. Arole, S. A. Micci-Barreca, S. Athavale, et al., "Annealing $Ti_3C_2T_z$ MXenes to Control Surface Chemistry and Friction," *ACS Applied Materials & Interfaces* 16, no. 5 (2024): 6290–6300, https://doi.org/10.1021/acsami.3c18232.

37. P. Zhang, H. Shou, Y. Xia, et al., "X-ray Insights into Formation of −O Functional Groups on MXenes: Two-Step Dehydrogenation of Adsorbed Water," *Nano Letters* 23, no. 4 (2023): 1401–1408, https://doi.org/10.1021/acs.nanolett.2c04712.

38. C. Huang, S. Shi, and H. Yu, "Work Function Adjustment of Nb_2CT_x Nanoflakes as Hole and Electron Transport Layers in Organic Solar Cells by Controlling Surface Functional Groups," *ACS Energy Letters* 6, no. 10 (2021): 3464–3472, https://doi.org/10.1021/acsenergylett.1c01656.

39. Z. Zhang, Z. Yao, X. Zhang, and Z. Jiang, "2D Carbide MXene under Postetch Low-Temperature Annealing for High–Performance Supercapacitor Electrode," *Electrochimica Acta* 359 (2020): 136960, https://doi.org/10.1016/j.electacta.2020.136960.

40. Q. Shan, Q. Ding, and W. Wu, "Preparation of Antioxidative MXene by Deep Eutectic Solvent-Assisted Electrochemical Ultrasonic Composite Exfoliation and Its Application in Flexible Solid-State Supercapacitors," *Industrial & Engineering Chemistry Research* 62, no. 24 (2023): 9492–9502, https://doi.org/10.1021/acs.iecr.3c00989.

41. M. Khazaei, M. Arai, T. Sasaki, A. Ranjbar, Y. Liang, and S. Yunoki, "OH-Terminated Two-Dimensional Transition Metal Carbides

16136829, 2026, 20, Downloaded from https://onlinelibrary.wiley.com/doi/10.1002/smll.202513542 by Yonghai Cao - South China University Of Technology , Wiley Online Library on [17/11/2026]. See the Terms and Conditions (https://onlinelibrary.wiley.com/terms-and-conditions) on Wiley Online Library for rules of use; OA articles are governed by the applicable Creative Commons License

and Nitrides as Ultralow Work Function Materials," *Physical Review B* 92, no. 7 (2015): 075411, https://doi.org/10.1103/PhysRevB.92.075411.

42. Y. Liu, H. Xiao, and W. A. Goddard III, "Schottky-Barrier-Free Contacts with Two-Dimensional Semiconductors by Surface-Engineered MXenes," *Journal of the American Chemical Society* 138, no. 49 (2016): 15853–15856, https://doi.org/10.1021/jacs.6b10834.

43. F. Pellegrino, L. Pellutiè, F. Sordello, et al., "Influence of Agglomeration and Aggregation on the Photocatalytic Activity of TiO_2 Nanoparticles," *Applied Catalysis B: Environmental* 216 (2017): 80–87, https://doi.org/10.1016/j.apcatb.2017.05.046.

44. R. Chen, C. Ni, J. Zhu, F. Fan, and C. Li, "Surface Photovoltage Microscopy for Mapping Charge Separation on Photocatalyst Particles," *Nature Protocols* 19, no. 8 (2024): 2250–2282, https://doi.org/10.1038/s41596-024-00992-2.

45. J. Zhu, S. Pang, T. Dittrich, et al., "Visualizing the Nano Cocatalyst Aligned Electric Fields on Single Photocatalyst Particles," *Nano Letters* 17, no. 11 (2017): 6735–6741, https://doi.org/10.1021/acs.nanolett.7b02799.

46. O. Chahib, Y. Yin, J. Liu, et al., "Probing Charge Redistribution at the Interface of Self-Assembled Cyclo-P_5 Pentamers on Ag(111)," *Nature Communications* 15, no. 1 (2024): 6542, https://doi.org/10.1038/s41467-024-50862-4.

47. K. Ozawa, M. Emori, S. Yamamoto, et al., "Electron–Hole Recombination Time at TiO_2 Single-Crystal Surfaces: Influence of Surface Band Bending," *The Journal of Physical Chemistry Letters* 5, no. 11 (2014): 1953–1957, https://doi.org/10.1021/jz500770c.

48. W. Gao, S. Li, H. He, et al., "Vacancy-Defect Modulated Pathway of Photoreduction of CO_2 on Single Atomically Thin $AgInP_2S_6$ Sheets into Olefiant Gas," *Nature Communications* 12, no. 1 (2021): 4747, https://doi.org/10.1038/s41467-021-25068-7.

49. R. Chen, S. Pang, H. An, et al., "Charge Separation via Asymmetric Illumination in Photocatalytic Cu_2O Particles," *Nature Energy* 3, no. 8 (2018): 655–663, https://doi.org/10.1038/s41560-018-0194-0.

50. J. Meng, C. Lee, and Z. Li, "Adjustment Methods of Schottky Barrier Height in One- and Two-Dimensional Semiconductor Devices," *Science Bulletin* 69, no. 9 (2024): 1342–1352, https://doi.org/10.1016/j.scib.2024.03.003.

51. D. Cai, Y. Gao, X. Wang, J. Yang, and S. Zhao, "Built-In Electric Field on the Mott–Schottky Heterointerface-Enabled Fast Kinetics Lithium–Sulfur Batteries," *ACS Applied Materials & Interfaces* 14, no. 34 (2022): 38651–38659, https://doi.org/10.1021/acsami.2c06676.

52. C. Zhang, C. Xie, Y. Gao, et al., "Charge Separation by Creating Band Bending in Metal–Organic Frameworks for Improved Photocatalytic Hydrogen Evolution," *Angewandte Chemie International Edition* 61, no. 28 (2022): 202204108, https://doi.org/10.1002/anie.202204108.

53. L. Wang, J. Sun, J. Shi, et al., "Reinforced Built-In Electric Field and Mediated Schottky Barrier Height via Carbon Quantum Dots Electronic Bridges on BiOBr/Ti_3C_2 for Efficient Photocatalytic Quinolone Antibiotics Degradation," *Chemical Engineering Journal* 500 (2024): 157168, https://doi.org/10.1016/j.cej.2024.157168.

54. X. Wang, B. Liu, S. Ma, et al., "Induced Dipole Moments in Amorphous ZnCdS Catalysts Facilitate Photocatalytic H_2 Evolution," *Nature Communications* 15, no. 1 (2024): 2600, https://doi.org/10.1038/s41467-024-47022-z.

55. N. Zhang, R. Long, C. Gao, and Y. Xiong, "Recent Progress on Advanced Design for Photoelectrochemical Reduction of CO_2 to Fuels," *Science China Materials* 61, no. 6 (2018): 771–805, https://doi.org/10.1007/s40843-017-9151-y.

56. C. Peng, X. Xie, W. Xu, et al., "Engineering Highly Active Ag/Nb_2O_5@Nb_2CT (MXene) Photocatalysts via Steering Charge Kinetics Strategy," *Chemical Engineering Journal* 421 (2021): 128766, https://doi.org/10.1016/j.cej.2021.128766.

57. S. Al Bacha, S. Saitzek, E. E. McCabe, and H. Kabbour, "Photocatalytic and Photocurrent Responses to Visible Light of the Lone-Pair-Based Oxysulfide $Sr_6Cd_2Sb_6S_{10}O_7$," *Inorganic Chemistry* 61, no. 46 (2022): 18611–18621, https://doi.org/10.1021/acs.inorgchem.2c03040.

58. Y. Li, S. Yu, J. Xiang, et al., "Revealing the Importance of Hole Transfer: Boosting Photocatalytic Hydrogen Evolution by Delicate Modulation of Photogenerated Holes," *ACS Catalysis* 13, no. 12 (2023): 8281–8292, https://doi.org/10.1021/acscatal.3c01210.

Supporting Information

Additional supporting information can be found online in the Supporting Information section.

Supporting File: smll72768-sup-0001-SuppMat.docx.

16136829, 2026, 20, Downloaded from https://onlinelibrary.wiley.com/doi/10.1002/smll.202513542 by Yonghai Cao - South China University Of Technology , Wiley Online Library on [17/11/2026]. See the Terms and Conditions (https://onlinelibrary.wiley.com/terms-and-conditions) on Wiley Online Library for rules of use; OA articles are governed by the applicable Creative Commons License